Journal of Materials Chemistry A

Accepted Manuscript

ROYAL SOCIETY OF CHEMISTRY

www.rsc.org/materialsA

Table of Contents Entry

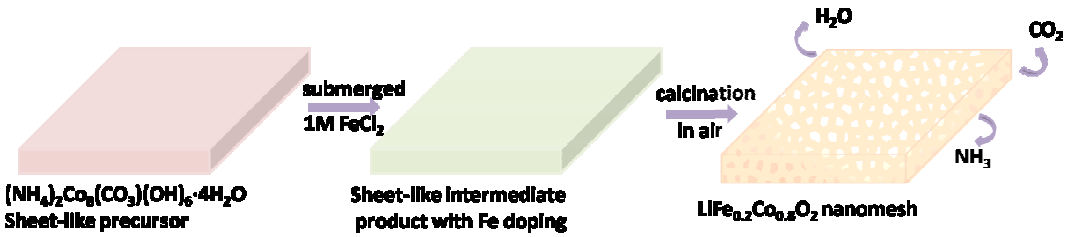

Herein, a one-step hydrothermal method, followed by Fe substitution and calcinations at 650 ^{o}C in air, has been applied to synthesize $LiFe_{0.2}Co_{0.8}O_2$ (LFCO) nanomeshes. Under the dual effect of doping and controlling morphology, the novel two-dimensional (2D) nanomeshes demonstrate enhanced performance as cathode materials for Li ion batteries (LIBs), for instance, high specific capacity, excellent capacity retention and superior rate performance. These enhancements result from the porous structure and the introduction of conductive Fe, which not only increases surface areas, but also decreases the electron transfer resistance. In the meantime, a large quantity of the selectively exposed (100), (010) and the equivalent crystal planes, the rapid rocking planes of Li^{+}, are of great benefit to accelerating lithiation-delithiation kinetics. To the best of our knowledge, no similar results have been reported before in synthesizing the layered LFCO nanomeshes for admirable Li storage performances.

Designed Synthesis of $LiFe_{0.2}Co_{0.8}O_2$ Nanomeshes to Greatly Improve the Positive Performance in Lithium-Ion Batteries

*Li Liu, Jida Chen, Yuanjuan Bai, Ling Fang, Huijuan Zhang, Yu Wang**

The State Key Laboratory of Mechanical Transmissions and the School of Chemistry and Chemical Engineering, Chongqing University, 174 Shazheng Street, Shapingba District, Chongqing City, P.R. China, 400044

E-mail: *wangy@cqu.edu.cn; prospectwy@gmail.com*

Supporting information for this article is available.

Keywords: $LiFe_{0.2}Co_{0.8}O_2$, Doping, Nanomeshes, Cathode, Lithium-ion battery

Abstract

The layered $LiFe_{0.2}Co_{0.8}O_2$ (LCFO) nanomeshes consisting of monocrystalline nanosized subunits, have been successfully achieved through an *in situ* doping and a template-sacrificial strategy. On account of the crystal mismatch between LFCO nanomesh and precursor being below 4.4%, the single crystal feature succeeded from the sheet-like precursor would be reasonably expectable. Meanwhile, the selectively exposed (100), (010) and equivalent crystal planes, the rapid rocking planes of Li^+, are close to 100%, implying the fast lithiation-delithiation kinetics. The introduction of the conductive Fe is beneficial to stabilizing the layered structure and decreasing the electron transfer resistance, leading to the high cyclability, excellent capacity retention of 92.5% after 200 cycles and superior rate performance, and delivering very high discharge capacities of 174, 167, 155,138 and 109 mAh g-1, respectively, at the rates of 0.1C, 1C, 2C, 5C and 10C. The special morphology and Fe doping jointly contribute to the enhanced electrochemical performance. To the best of our knowledge, no similar results have been reported before in synthesizing the layered LFCO nanomeshes for LIBs with admirable Li storage performances.

Introduction

With the quick exhaustion of fossil fuels and the following urgent need to address the environmental problems associated with their uses, the development of clean, safe, and renewable energy sources has been paid a great deal of attention around the world.[1-3] Due to the limitation of time and space for traditional clean energy, it's necessary to seek for a new energy storage devices.[4] Among all the electrical energy storage mediums, the lithium-ion batteries (LIBs) is evidenced to be a promising candidate, which is the dominant power source for portable electronics, electric vehicles (EVs), hybrid electric vehicles (HEVs), and stationary energy storage.[1] The cathode materials of LIBs are believed to have a significant influence on the electrochemical performance. In order to comply with the consumers' demands, such as higher storage capacity, shorter recharging times, greater cycling stability, and higher power output,[5] all kinds of cathode materials have been investigated e.g. $LiCoO_2$,[6] $LiMn_2O_4$,[7] $LiFePO_4$,[8] ternary composite materials.[9] Among these candidates, owing to its high voltage and ideal capacity retention, the layered intercalation compound of $LiCoO_2$ remains as the foundation cathode material in commercial application on a large scale, despite its high price and slight toxicity.[10] The layered structure of $LiCoO_2$ allows Li^+ ions to be removed from the cathode and inserted in the anode during the charging process, and vice-versa during the discharging process, respectively. As a widely commercialized cathode material for LIBs, $LiCoO_2$ possesses a high theoretical capacity of 274 mAh g^{-1}, when all the lithium ions are recycled.[11, 12] Nevertheless, because of

undergoing the phase transformation, the layered structure of $LiCoO_2$ is easily collapsing at x>0.5 ($Li_{1-x}CoO_2$).[13, 14] Thus, its practical capacity is ~140 mAh g^{-1} in the voltage window of 2.7-4.2V, which is half of its theoretical capacity. Although this high capacity of $LiCoO_2$ seems attractive from battery's point of view, actually only 50% of the Li^+ could be recycled, thus limiting the performance of $LiCoO_2$.[15] As a result, the specific capacity, energy and powder densities of lithium-ion batteries with $LiCoO_2$ as the cathode are restrained.

In order to enhance the practical capacity or cycling stability of the $LiCoO_2$ electrodes at the high voltages, a lot of modifications have been attempted,[16] such as metal ion doping,[17, 18] surface modification,[19] preparing nanocomposite[20] and fabricating nano-sized materials.[21] Doping metal ion seems to be the most acceptable approach for commercial exploitation considering the production cost, notwithstanding the fact that only some of these modifications could lead to good capacity retention. According to R. Alcantara et al,[22] $LiCoO_2$ in doping with metal ions (M) could stabilize the layered framework, which will strengthen the cyclability and improves the capacity of the electrochemical cell of Li//$LiCo_{1-z}M_zO_2$. Extensive investigations into cation doping using Mg,[23-25] Al,[26] Sn,[27] Ni,[28] Mn,[29] and so forth are readily available in the literature. As is well known, non-transition metal doping could enhance voltage at the expense of capacity, while transition metal doping of $LiCoO_2$ would increase capacity theoretically.[30] For this reason, it's feasible to partially substitute the transition metal cation in $LiCoO_2$. On the other hand, mounting experimental results have suggested that decreasing the particle size by nanostructuring $LiCoO_2$ can render high charge-discharge rates as a result of increasing electrode-electrolyte contact area and shortening migration pathway for Li^+ transport.[31-33] Therefore, controlling the morphology is another important method to improve the performance of LIBs.[34]

In this work, the layered-structure $LiFe_{0.2}Co_{0.8}O_2$ (LFCO) nanomesh has been successfully synthesized for the first time based on doping of transition metal ion Fe^{3+} and controlling the morphology. The LFCO nanomesh is composed of interconnected nanosized subunits with highly porous and single-crystal structure. The grain refinement provides more crystal boundaries, shorter distances for Li^+ diffusion and larger electrode-electrolyte contact areas for Li^+ thorough flux across the interface, leading to better rate capability. Most importantly, the void space in the novel 2-dimentional (2D) nanomesh structure may digest the local volume change during the lithium insertion/extraction, thus facilitating the structural stability of the electrode material and improving the cyclability. From another aspect, substitution of Fe for Co can enhance the cycling properties of $LiCoO_2$ by strongly increasing the electronic conductivity of the pristine $LiCoO_2$. In addition, the Fe^{3+} ions could move to the inter-slab space along with Co^{3+} ions. Then they locate at the site of Co assisting the movement of Li^+ ions by preventing the vacancy ordering, triggering improvements in the specific capacity. Taken together, our research reveals that the electrode made of these LFCO nanomeshes exhibits high capacity, excellent cyclability, and superior rate capability at room temperature. To the best of our knowledge, this is the first report on $LiFe_{0.2}Co_{0.8}O_2$ with nanomesh structure as the cathode materials. Thus, the present work may offer a new strategy based on *in situ* doping and template-sacrificial reactions for the design of high-performance cathode materials with nanomesh structure for LIBs applications.

Results and Discussion

The fabrication process of highly porous LFCO nanomesh is schematically illustrated in Scheme. 1. The $(NH_4)_2Co_8(CO_3)_6(OH)_6 \cdot 4H_2O$ precursors with a sheet-like morphology, as "sacrificial" templates, were first synthesized by a hydrothermal method. They were then submerged in 1M $FeCl_2$ aqueous solution at room temperature for 10 h. In the process, Fe^{2+} diffused into the inter-planar spacing and substituted Co^{3+} *in situ*. Subsequently, the solid-state reaction between the above sheet-like "sacrificial" templates and the lithium hydroxide at the molar ratio of 1:1.1 was carried out at 650 ^oC in a muffle furnace. At the moment, Fe^{2+} is oxidized to Fe^{3+} under air atmosphere. Meanwhile, a large number of pores within the LFCO nanomesh were achieved due to the release of CO_2, H_2O and NH_3 gas. For a comparison, we also synthesized LFCO bulks and $LiCoO_2$ particles

without doping Fe.

To identify the crystallinity and crystal phase, we performed powder X-ray diffraction (XRD) analysis on the as-prepared products. The XRD pattern (Fig. S1 support information) reveals that the precursor of $(NH_4)_2Co_8(CO_3)_6(OH)_6{\cdot}4H_2O$ is highly crystalline. All of the diffraction peaks can be easily indexed to the hexagonal phase of $(NH_4)_2Co_8(CO_3)_6(OH)_6{\cdot}4H_2O$ (JCPDS No. 52-0552). After Fe doping at room temperature, the crystal structures don't change, as shown in Fig. S1. Fig. 1 shows the representative XRD patterns for the LFCO nanomeshes, LFCO bulks and pristine $LiCoO_2$ particles. All the diffraction peaks can be readily assigned to well-crystallized hexagonal $LiFe_{0.2}Co_{0.8}O_2$ (JCPDS No. 52-0664) and $LiCoO_2$ (JCPDS No. 75-0532). No other peaks were observed for impurities. Notably, for LFCO nanomeshes and LFCO bulks, all the diffraction peaks slightly moved to the low angle positions, compared with those of pristine $LiCoO_2$. The main reason for the shift is the difference in ionic radius between Fe^{3+} and Co^{3+}, which are 0.76 Å and 0.63 Å, respectively. As we all know, the ionic radius of Li^+ is 0.60 Å. Since the ionic radius of Fe^{3+} (0.76 Å) is closed to that of Co^{3+}, it could be expected that Fe^{3+} will preferably substitute for Co^{3+} in $LiCoO_2$. When the Fe^{3+} migrated into the layered structure of the $LiCoO_2$, the crystal lattice parameters have a large change in *c*-axis versus a tiny change in *a*-axis. These changes generate the shift of diffraction peaks. Throughout all the synthesis, X-ray diffraction (XRD) technique is always utilized to trace down the transformation process and has successfully recorded the overall transition from $(NH_4)_2Co_8(CO_3)_6(OH)_6{\cdot}4H_2O$ sheets to LFCO nanomesh, further certifying the rationality of the designed synthesis.

The morphology and microstructure of the products were examined by field-emission scanning electron microscope (FESEM). According to Fig. 2a, the as-prepared precursors exhibit a 2D sheet-like shape, with lengths of 2-5 μm and widths of 1-2 μm. The thickness of the precursor with smooth surface is determined to be about 20 nm. The SEM in Fig. 2b displays that the calcined products exhibit uniformity and continuity, meanwhile, the individual nanomesh is isolated and separated from each other. We can see the dimensions of those calcined products are from several hundreds of square nanometers to tens of square micrometers. Apparently, the material morphology is essentially preserved during the solid-state reaction process, which also implies the architectural framework is pretty stable. From the inset image in Fig. 2b, it can be observed that the thickness is estimated to be 20-30 nm, which reveals a short lithium ion diffusion pathway compared with the as-prepared LFCO bulks and $LiCoO_2$ particles. Fig. 2c indicates that LFCO nanomesh is composed of the interconnected nanosized subunits with highly porous structure. In addition, the surface of LFCO nanomesh is no longer smooth, but becomes much rougher in contrast to the precursors. We have also synthesized the SEM images of LFCO bulks and $LiCoO_2$ particles, shown in the Fig. S2a and S2b. The X-ray energy dispersive spectrum (EDS) (Fig. 2d) indicates the LFCO nanomeshes contain Fe, Co, O, Si and C elements, wherein the Si element comes from the silicon substrates and the C element is from the air. The Fe/Co ratio obtained from EDS is close to 1:4, in good agreement with the XRD results. For LFCO bulks, the same results have been obtained from the EDS image in Fig. S2c.

As a powerful microstructural characterization tool, transmission electron microscopy (TEM) was adopted to highlight the unique structure in the ultimately obtained samples as shown in Fig. 3. Fig. 3a shows the typical bright-field TEM image for the sheet-like precursors. The wrinkle can be distinctly observed in the Fig. 3a, certifying that the sheet-like precursors are particularly thin. From Fig. 3b-3d, the gradually magnified TEM images are described in sequence. The morphology of the as-synthesis LFCO nanomesh is exhibited in Fig. 3b. Obviously, the sheet-like shape is retained after thermal decomposition and crystal transformation. Fig. 3c is the magnified TEM image which shows that the as-synthesis LFCO nanomesh contains many voids with irregular size, as the black circles indicated. From the TEM images, a distinct light-dark contrast is observed in the nanomesh, indicating the existence of penetrating pore spaces. On the contrary, there is no pores' distribution in the sheet-like precursors. It is believed that these porous spaces may function as channels to facilitate the electrolyte's diffusion

and Li ions' exchange. Fig. 3d further verifies the LFCO nanomesh is composed of interconnected nanosized subunits with highly porous spaces and the average diameter of those pores is ranging 30 to 60 nm.

High-resolution transmission electron microscope (HRTEM) images of $(NH_4)_2Co_8(CO_3)_6(OH)_6{\cdot}4H_2O$ sheet-like precursor and LFCO nanomesh, shown in Fig. 4a and 4b, provide clearer insight into the microstructures of the products. The HRTEM image of precursor, demonstrated in Fig. 4a, verifies the single crystalline nature with an interlayer spacing of about 0.45 nm, which is well consistent with the (002) crystal plane of $(NH_4)_2Co_8(CO_3)_6(OH)_6{\cdot}4H_2O$. Fig. 4b provides the powerful evidence that the LFCO nanomesh is composed of the successive crystal lattices. The lattice inter-distance is calculated to be 0.47 nm, and agrees well with that of (003). Prof. Wang, et al has investigated that along the specific directions of [100] and [010], Li^+ can diffuse inward and outward the bulk of material without big obstacle according to the atomic modeling of $LiCoO_2$.[35] In this regard, the exposed planes are clearly observed and fixed as the equivalent planes of (010) or (100), both of which finally account for almost 100% surface ratio in LFCO nanomesh. In accordance with Fig. 4a and Fig. 4b, it can be calculated that the crystal mismatch is below 4.4%, from $(NH_4)_2Co_8(CO_3)_6(OH)_6 \cdot 4H_2O$ sheet-like precursor to LFCO nanomesh, suggesting another powerful evidence for the single crystal feature. Prof Wang, et al. has explained that it's actually a thermodynamic-equilibrium product without any necessity to conquer the energy gap, which is usually required when conventionally transformed from the thermodynamically stable (001) to kinetically dominated (010) in $LiCoO_2$.[26] Similarly, the LFCO nanomeshes display the equivalent planes of (010) and (100), implying the LFCO nanomesh also possesses the rapid rocking planes of Li^+. As a consequence of this fact, the electrochemical performance will be tremendously enhanced. The EDS mapping images shown in Fig. S3 reveal the homogeneous compositions of the LFCO nanomesh, in which a phase separation of Co, Fe and O components is not observed. In order to confirm the LFCO nanomesh's surface area and pore size distribution, the Brunauer-Emmett-Teller (BET) method is used for further measurement. The nitrogen absorption-desorption isotherm and the pore size distribution profiles are shown in Fig. 4c and the inset image, respectively, to display that the surface area of LFCO nanomeshes is 42.8 $m^2\ g^{-1}$ and the pore size is mainly narrowed around 38.23 nm. This suggests that the as-prepared LFCO nanomeshes may exhibit a good performance for electrolyte flooding and Li^+ insertion. On the contrary, the surface area of $LiCoO_2$ particles, shown in Fig. 4d, is 5.149 $cm^2\ g^{-1}$. From the inset image of Fig. 4d, it can be seen that the $LiCoO_2$ particles are almost without any pores.

The electrochemical performances of LFCO nanomeshes is investigated using Li metal as anode at various current densities between 3.0 and 4.4 V *vs.* Li/Li^+. Fig. 5a shows the charge-discharge curves of LFCO nanomeshes for different cycles at a rate of 0.1 C (1 C = 274 mA g^{-1}). All of the smooth charge and discharge profiles suggest that the electrode structures are stable in the voltage range. The initial galvanostatic charge and discharge capacities of LFCO nanomeshes are 183.5 and 175.2 mAh g^{-1}, respectively, which is superior to those previously reported in literature for Mn-doped $LiCoO_2$ (156 mAh g^{-1} at the current density of 20 mA g^{-1}) [36], Ti-doped $LiCoO_2$ (154.7 mAh g^{-1} at 30 mA g^{-1}) [37] and Mg-doped $LiCoO_2$ (147 mAh g^{-1} at 30 mA g^{-1})[38]. The initial capacity loss of the LFCO nanomesh cathodes during the first cycle may be attributed to the formation of a solid-electrolyte-interface (SEI) film. The discharge capacities at the 2^{nd}, 50^{th}, 100^{th} and 200^{th} cycles are approximately 174, 171, 168 and 161 mAh g^{-1}, respectively. Thus, the charge-discharge curves indicate outstanding capacity retention of LFCO nanomesh, suggesting Fe-doping is found to be useful in stabilizing the layered structure. Usually, the layered $LiCoO_2$ shows the discharging voltage above 3.8 V, as previously reported[6, 39, 40]. It's interesting to note the phenomenon of appearing another voltage plateau in the discharge curves, which is normally observed for transition metal substitution and well-documented in the literature[41]. Such a result is generally attributed to the redox reaction of transition metal ion. A voltage plateau of discharge is almost parallel to 3.9 V *vs* Li^+/Li, corresponding to the redox couple of Co^{3+}/Co^{2+}. Notably, the voltage plateau of LFCO nanomeshes is little higher than that of $LiCoO_2$ because of Fe substitution. Another voltage plateau around 3.4 V is

observable, corresponding to the redox reaction between the Fe^{3+} and Fe^{2+}. Cyclic voltammetry plays a key role in electrochemical characterizations, which enables the scanning of the potential of working electrode in both anodic and cathodic directions. Fig. 5b reveals the cyclic voltammograms (CVs) of the LFCO nanomeshes during the first three cycles measured at a scan rate of 0.1 mV s^{-1} in the voltage range 3.0-4.4 V. The variation in current densities and potential peak positions between the first and second cycles, displayed in Fig. 6b, is ascribed to the irreversible formation of the solid-electrolyte interface (SEI), resulting in the capacity loss, which is also verified in Fig. S4. Except for the first cycle, all of the curves in the subsequent cycles follow the same path, indicating high stability and reversibility for Li^+ insertion and extraction. The reduction peaks at ~3.9 V and 3.4 V in the cycles are attributed to the reduction of Co^{3+} to Co^{2+} and Fe^{3+} to Fe^{2+}, respectively. The oxidation peak at ~4.1V corresponds to the oxidation of Co^{2+} to Co^{3+}. Fig. 5c presents the coulombic efficiency, specific capacity and stability upon 200 cycles at a rate of 0.1 C. It's interesting to observe that the charge and discharge capacities decrease slightly even after 200 cycles. Also, from the second cycle onwards, the charge capacity can be retained at ~170 mAh g^{-1} and the discharge capacity of the LFCO nanomeshes remains ~161 mAh g^{-1}, with a high coulombic efficiency of around 93-96% after 200 cycles, which is closed to that of $LiCo_{0.998}Ti_{0.002}O_2$ (95%) in literature[37]. To our surprise, the coulombic efficiencies of the first several cycles are relatively lower than those of the subsequent cycles. The possible reason is that the active materials don't completely contact with electrolyte in the first several cycles, causing the capacity's decrease. As the redox reaction proceeds, the electrolyte penetrates into the inner part of the void space, resulting in the increased capacities. Therefore, the specific capacity is beyond the theoretical value of 140 mAh g^{-1} of commercial $LiCoO_2$ cathode, indicating excess Li^+ (>50%) can be reversibly intercalated, which is ascribed to the fact that Fe enters the layered $LiCoO_2$ to stabilize the layered structure. On the contrary, the LFCO bulks and $LiCoO_2$ particles display a poor performance in capacity retention, shown in Fig. S4. From Fig. S4, we can see the discharge capacities of the $LiCoO_2$ particles and LFCO bulks decrease 88 and 54 mAh g^{-1} after 200 cycles, and the capacity retention is about 46.5% and 68.1%, respectively. However, the discharge capacity only decreases by 13 mAh g^{-1} after 200 cycles and the capacity retention of the LFCO nanomeshes remain 92.5%. Those results are better than that of Zr-doped (80 % after 60 cycles) [23], Mn-doped (85.55 % after 100 cycles) [36] and Mg-doped (63.4 % after 100 cycles) [42] $LiCoO_2$ particles, which indicates that superior cycling stability is achieved with the Fe-doping and designing morphology. Fig. S5 shows the SEM image of LFCO nanomeshes after electrochemical testing. Although the aggregation of LFCO nanomeshes is observed, the nanomesh structure has been reserved after 200 cycles, further supporting the claims of the eminent stability and cyclability. We have also studied the rate performance of the LFCO nanomeshes, LFCO bulks and $LiCoO_2$ particles, because of its importance in evaluating the total performance. As shown in Fig. 5d, the current densities are risen stepwise through a series of different current densities to as high as 10 C. When the LFCO nanomesh electrode is first cycled at 0.1 C, the discharge capacity is stabilized at 174 mAh g^{-1} after 10 cycles. Subsequently, when the current densities gradually increase to 1 C, 2 C, 5 C and 10 C for 10 cycles, respectively, the corresponding average specific capacities of 167, 155, 138 and 109 mAh g^{-1} are obtained at each of these current densities. Upon the high-rate charge-discharge cycling, the current density is cycled back to 0.1 C, with a specific capacity of 166 mAh g^{-1} recovered and the capacity retention of 95.4% obtained, indicating the enhanced rate performance and cyclability for LFCO nanomeshes. At the rates of 0.1, 1, 2, 5 and 10 C, by contrast, the specific capacities are 156, 144, 117, 85 and 68 mAh g^{-1} for LFCO bulks, versus 143, 130, 102, 66 and 43 mAh g^{-1} for $LiCoO_2$ particles, respectively. When the current density returns to 0.1 C, the specific capacities of LFCO bulks and $LiCoO_2$ particles are 145 and 118 mAh g^{-1}, respecitively. Obviously, the rate performance of LFCO bulks and $LiCoO_2$ particles is inferior to that of LFCO nanomeshes. Meanwhile, at the same current densities, the specific capacities of LFCO bulks and $LiCoO_2$ particles quickly decay for 10 charge-discharge cycles, compared to LFCO nanomeshes.

In order to understand the advantages on the electrochemical performance for LFCO nanomeshes,

alternating-current (AC) impedance measurements are carried out and the corresponding Nyquist plots are shown in Fig. 6. The Nyquist plots consist of three parts: 1) a high-frequency intercept on the real Z' axis, 2) a semicircle in the high-to-medium-frequency region and 3) a straight line at the very low-frequency region. Both data were analyzed using equivalent circuit exhibited in the inset of Fig.6, where the high-frequency intercepts for both LFCO nanomeshes and $LiCoO_2$ particles are almost zero, suggesting that they have the same combination resistance (R_{sf}) incorporated with the ionic resistance of the electrolyte and the contact resistance between the active material and the current collector.[43] The charge-transfer resistance associated with the high-to-medium-frequency semicircle, R_{ct}, is related to Li^+ transportation across the active mass interface.[44] The values calculated from the diameters of the high-to-medium-frequency semicircles in the Nyquist plots for the electrodes are summarized in Table 1. Here, the influence of Fe-doping on the value of R_{ct} is interesting. From Table 1, it can be seen that R_{ct} of $LiCoO_2$ particles increases from 181.5 at the 10^{th} cycle to 314 at the 200^{th} cycle, with a gain of around 73%. However, for the LFCO nanomeshes, the increment of the electrochemical resistance after 200 cycles is much smaller than that of the non-doping $LiCoO_2$ particles and the lately reported for Mg-doped $LiCoO_2$[42]. The EIS characterization further reveals that the increase of charge transfer resistance during cycling has successfully been suppressed by the substitution of Fe.

The improved electrochemical performance of the LFCO nanomeshes might be attributed to two factors. On one hand, the novel 2D LFCO nanomesh, composed of the interconnected monocrystalline nanosized subunits, will provide a short pathway for lithium ion diffusion and then decrease the lithium-ion diffusion resistance. In the meantime, the existence of pore space in the LFCO nanomeshes could reduce the inner pressure and enlarge the electrode-electrolyte contact areas for Li^+ migration across the interface, resulting in an excellent rate capacity. Furthermore, the pore space could significantly maintain the structure's integrity by partly mitigating the mechanical strain induced by volume change associated with the repeated Li^+ insertion and extraction process during cycling, which might greatly contribute to the excellent cycle stability. In addition, it's worth noting that Li^+ rapid diffusion planes of (010) and (100) overwhelmingly dominate the exposed surface areas with approximately 100% ratio, which builds up a large amount of express routes for Li^+ rocking in a reversible way. On the other hand, owing to the fact that $LiCoO_2$ and $LiFeO_2$ belong to the same crystal structure, the solid solution could be formed. Therefore, the Fe ions can diffuse into the interplanar spacing of $LiCoO_2$ and substitute Co *in situ*, improving the stability and cyclability during the de-intercalation of Li^+ ions. Upon the substitution of Co by Fe, the lattice parameters of *a* and *c* increase (large increase in *c*-axis *versus* small change in *a*-axis) as well so that a more open lattice structure is evolved and the lithium ion can insert and extract more easily. What's more, Fe possesses excellent electronic conductivity, the introduction of Fe into $LiCoO_2$ can decrease the charge transfer resistance, indicating an enhancement in the electrochemical kinetics and the consequent improvement in high-rate capabilities. This is the main reason that the electrochemical performances of Fe-doped $LiCoO_2$ are superior to those of other metal ions doped $LiCoO_2$. Meanwhile, the enhanced discharge capacity can also be ascribed to the Fe doping, for the reason that excess Li^+ (>50%) could be recycled from the stable framework.

Conclusion

In summary, layer-structured LFCO nanomeshes have successfully been synthesized through *in suit* transition metal ion doping and a template-sacrificial route by using sheet-like precursors as the template. From the sheet-like precursors to LFCO nanomeshes, the crystal mismatch is less than 4.4%. The porous LFCO nanomesh is composed of interconnected monocrystalline subunits and displays a high specific surface area of 42.8 m^2 g^{-1} with a pore distribution of 38.23 nm, promoting electrolyte penetration into active materials. The selectively exposed (100), (010) and the equivalent crystal planes are almost 100% surface ratio and in favour of Li^+ diffusion inward and outward. After Fe substitutes Co, Fe ions are favorable for enhancing the stability of structural framework, in the meantime, excess Li^+ (>50%) can be utilized, leading to high specific capacity. When applied as cathode

material for LIBs, the LFCO nanomeshes exhibit a large reversible capacity (161 mAh g^{-1} after 200 cycles), excellent cyclability with capacity retention of 92.5%, improved lithiation-delithiation kinetics and superior rate capability. It's noted that controlling morphology and transition metal doping can be extended to other cathode materials for advanced LIBs. Undoubtedly, this research will be of great significance in improving LIBs efficiency.

Experimental Section

Materials: All chemicals or materials were utilized directly without any further purification before use: ethylene glycol (Fisher Chemical, 99.99 %), ammonium hydroxide ($NH_3 \cdot H_2O$, 28–30 wt %, J. T. Baker), cobalt nitrate ($Co(NO_3)_2 \cdot 6H_2O$, 99.9 %, Aldrich), sodium carbonate (Na_2CO_3,99.9 %, Aldrich), ferrous chloride ($FeCl_2$, 99.9 %, Aldrich), and Lithium hydrate ($LiOH \cdot H_2O$, 99.9 %, Aldrich), cobalt oxide (Co_3O_4, 99.9 %, Aldrich), ferric oxide (Fe_2O_3, 99.9 %, Aldrich) and anhydrous ethanol (Fisher Chemical, 99.99 %).

Preparation of $(NH_4)_2Co_8(CO_3)_6(OH)_6 \cdot 4H_2O$ nanosheets: $(NH_4)_2Co_8(CO_3)_6(OH)_6 \cdot 4H_2O$ nanosheets were synthesized by a hydrothermal reaction. Ethylene glycol (12.5 mL), concentrated $NH_3 \cdot H_2O$ (12.5 mL), 1M Na_2CO_3 aqueous solution (5 mL), and 1M $Co(NO_3)_2$ aqueous solution (5 mL) were mixed step-by-step under strong stirring with intervals of 1-2 min. After that, the precursor solution was stirred for another 20 min. Then, the mixture changed into a deep pink-violet homogeneous solution. Once the mixture solution was transferred into a Teflon-lined stainless steel autoclave at a volume of 45 mL, a thermal treatment was performed for the Teflon-liner in an electric oven at 170 ^oC for 17 h. After the autoclave was cooled down naturally to room temperature in air, samples deposited at the bottom were collected and washed by centrifugation for at least three cycles by using deionized water (D.I. water) and two cycles by using pure ethanol. Finally, the as-synthesized samples were then dried in a vacuum oven at 600 ^oC overnight to remove the absorbed water for the subsequent fabrication and characterizations.

Preparation of the $LiFe_{0.2}Co_{0.8}O_2$ nanomeshes: $(NH_4)_2Co_8(CO_3)_6(OH)_6 \cdot 4H_2O$ nanosheets (100 mg) were soaked in 1M $FeCl_2$ (25mL) aqueous solution for 10h. Then, the mixture was shocked every ten minutes. In the process, the aqueous solution changed from a bright green into pink and the samples changed from silver aubergine into reseda. Then, the samples were centrifugation for at least three cycles by using deionized water (D.I. water) and two cycles by using pure ethanol. Following that, the as-synthesized samples were dried in a vacuum oven at 60 ^oC overnight. $(NH_4)_2Co_8(CO_3)_6(OH)_6 \cdot 4H_2O$ nanosheets, which doped with Fe, were converted to LFCO nanomeshes when reacted with over stoichiometric molar ratio of $LiOH \cdot H_2O$ at 650 ^oC for 200 min under air atmosphere in a muffle furnace.

Preparation of the $LiFe_{0.2}Co_{0.8}O_2$ bulks and the $LiCoO_2$ particles: The Co_3O_4 powders and Fe_2O_3 powders were mixed with $LiOH \cdot H_2O$ by ball milling in molar ratios of 8: 3: 30. Then the mixture was annealed at 700 ^oC under air atmosphere for 200 min in a muffle furnace to obtain the LFCO bulks. The pristine $LiCoO_2$ particles were prepared under the same reaction conditions with a molar ratios of 1: 3 (Co_3O_4: $LiOH \cdot H_2O$).

Characterization of the samples: field-emission SEM (JEOL JSM-7800F) coupled with an EDS analyzer (JEOL, JSM-7600F), TEM coupled with an EDX analyzer (Philips, Tecnai, F30, 300 kV), powder X-ray diffraction (Bruker D8 Advance X-ray diffractometer with Co Ka radiation (λ = 1.78897 Å)), Brunauer-Emmett-Teller surface area measurement (BET, Quantachrome Autosorb-6B surface area and Pore size analyzer)

Electrochemical testing: A homogeneous mixture composed of LFCO nanomeshes, carbon black, and polyvinyl difluoride (PVDF) using 1-methyl-2-pyrrolidinone (NMP) as solvent in a weight ratio of 80:15:5 was prepared under strong magnetic stirring for at least 1 d. Then some of the mixture was extracted and spread onto Al foils. Before and after the samples were spread, the Al foils were weighed using a high-precision analytical balance. The read difference was the exact mass for the coated samples on Al foils. Normally, the sample loadings range from 1.2 to 1.6 $mg \cdot cm^{-2}$. The obtained pieces of Al covered with samples were then used as working electrodes with 1M $LiPF_6$ in ethylene carbonate and diethyl carbonate (EC/DMC=1:1 v/v) as electrolyte. Celgard 2400 was applied as the separator film to isolate the two electrodes. Pure Li foil (99.9%, Aldrich) served as the counter electrode and reference electrode. The cell was assembled in an argon filled glove box in which moisture and oxygen concentrations were strictly limited to below 0.1 ppm. The galvanostatic cycling was performed using a Neware

battery testing system (model 5V 5mA), and CV data was collected using an Autolab (model AUT71740) in a three-electrode cell.

Acknowledgements

This work was financially supported by the Thousand Young Talents Program of the Chinese Central Government (Grant No.0220002102003), National Natural Science Foundation of China (NSFC, Grant No. 21373280，21403019), Beijing National Laboratory for Molecular Sciences (BNLMS) and Hundred Talents Program at Chongqing University (Grant No. 0903005203205).

References and Notes:

1. J. B. Goodenough and Y. Kim, *J. Power Sources.*, 2011, **196**, 6688-6694.
2. J. M. Tarascon and M. Armand, *Nature.*, 2001, **414**, 359-367.
3. M. Armand and J. M. Tarascon, *Nature.*, 2008, **451**, 652-657.
4. P. He, H. Yu, D. Li and H. Zhou, *J. Mater. Chem.* , 2012, **22**, 3680-3695.
5. B. A. Johnson and R. E. White, *J. Power Sources.*, 1998, **70**, 48-54.
6. M. Okubo, E. Hosono, J. Kim, M. Enomoto, N. Kojima, T. Kudo, H. S. Zhou and I. Honma, *J. Am. Chem. Soc.* , 2007, **129**, 7444-7452.
7. Y. Koyama, T. E. Chin, U. Rhyner, R. K. Holman, S. R. Hall and Y. M. Chiang, *Adv. Funct. Mater.*, 2006, **16**, 492-498.
8. K. Saravanan, P. Balaya, M. V. Reddy, B. V. R. Chowdari and J. J. Vittal, *Energ Environ. Sci.*, 2010, **3**, 457-463.
9. J. Xiao, X. Chen, P. V. Sushko, M. L. Sushko, L. Kovarik, J. Feng, Z. Deng, J. Zheng, G. L. Graff, Z. Nie, D. Choi, J. Liu, J.-G. Zhang and M. S. Whittingham, *Adv. Mater.*, 2012, **24**, 2109-2116.
10. R. Alcántara, P. Lavela, J. L. Tirado, R. Stoyanova and E. Zhecheva, *J. Solid State Chem.*, 1997, **134**, 265-273.
11. J. Fan and P. S. Fedkiw, *J. Power Sources.*, 1998, **72**, 165-173.
12. A. Manthiram and J. Kim, *Chem. Mater.*, 1998, **10**, 2895-2909.
13. J. N. Reimers and J. R. Dahn, *J. Solid State Chem.*, 1992, **139**, 2091-2097.
14. M. Menetrier, I. Saadoune, S. Levasseur and C. Delmas, *J. Mater. Chem.* , 1999, **9**, 1135-1140.
15. Z. H. Lu, D. D. MacNeil and J. R. Dahn, *Electrochem.Solid-State Lett.*, 2001, **4**, A191-A194.
16. J.-H. Shim, S. Lee and S. S. Park, *J. Am. Chem. Soc.*, 2014, **26**, 2537-2543.
17. Y. Wu and A. Manthiram, *Solid State Ionics.*, 2009, **180**, 50-56.
18. Q. Y. Wang, J. Liu, A. V. Murugan and A. Manthiram, *J. Mater. Chem.* , 2009, **19**, 4965-4972.
19. J. Zheng, S. Deng, Z. Shi, H. Xu, H. Xu, Y. Deng, Z. Zhang and G. Chen, *J. Power Sources.*, 2013, **221**, 108-113.
20. J. Wang, B. Qiu, H. Cao, Y. Xia and Z. Liu, *J. Power Sources.*, 2012, **218**, 128-133.
21. Z. He, Z. Wang, H. Guo, X. Li, W. Xianwen, P. Yue and J. Wang, *Mater. Lett.*, 2013, **91**, 261-264.
22. T. Ohzuku, A. Ueda, M. Nagayama, Y. Iwakoshi and H. Komori, *Electrochim. Acta.*, 1993, **38**, 1159-1167.
23. F. Nobili, F. Croce, R. Tossici, I. Meschini, P. Reale and R. Marassi, *J. Power Sources.*, 2012, **197**, 276-284.
24. S. Levasseur, M. Ménétrier and C. Delmas, *Chem. Mater.*, 2002, **14**, 3584-3590.
25. R. Z. Yin, Y. S. Kim, S. J. Shin, I. Jung, J. S. Kim and S. K. Jeong, *J. Electrochem. Soc.*, 2012, **159**, A253-A258.
26. F. Zhou, W. B. Luo, X. M. Zhao and J. R. Dahn, *J. Electrochem. Soc.*, 2009, **156**, A917-A920.
27. C. D. W. Jones, E. Rossen and J. R. Dahn, *Solid State Ionics.*, 1994, **68**, 65-69.
28. I. Saadoune and C. Delmas, *J. Solid State Chem.*, 1998, **136**, 8-15.
29. C. Julien, M. A. Camacho-Lopez, T. Mohan, S. Chitra, P. Kalyani and S. Gopukumar, *Solid State Ionics.*, 2000, **135**, 241-248.
30. S. Venkatraman, V. Subramanian, S. Gopu Kumar, N. G. Renganathan and N. Muniyandi, *Electrochem. Commun.*, 2000, **2**, 18-22.
31. Y.-G. Guo, J.-S. Hu and L.-J. Wan, *Adv. Mater.*, 2008, **20**, 2878-2887.

32. A. S. Arico, P. Bruce, B. Scrosati, J.-M. Tarascon and W. van Schalkwijk, *Nat. Mater.*, 2005, **4**, 366-377.
33. P. G. Bruce, B. Scrosati and J.-M. Tarascon, *Angew. Chem. Int. Ed.*, 2008, **47**, 2930-2946.
34. T. Wei, R. Zeng, Y. Sun, Y. Huang and K. Huang, *Chem. Commun.*, 2014, **50**, 1962-1964.
35. H. J. Zhang, C. C. Wong and Y. Wang, *Cryst Growth Des.*, 2012, **12**, 5629-5634.
36. D. Luo, G. Li, C. Yu, L. Yang, J. Zheng, X. Guan and L. Li, *J. Mater. Chem.* , 2012, **22**, 22233-22241.
37. J. Yu, Z. Han, X. Hu, H. Zhan, Y. Zhou and X. Liu, *J. Power Sources.*, 2014, **262**, 136-139.
38. M. V. Reddy, T. W. Jie, C. J. Jafta, K. I. Ozoemena, M. K. Mathe, A. S. Nair, S. S. Peng, M. S. Idris, G. Balakrishna, F. I. Ezema and B. V. R. Chowdari, *Electrochim. Acta.*, 2014, **128**, 192-197.
39. H. Chen and C. P. Grey, *Adv. Mater.*, 2008, **20**, 2206-2210.
40. X. X. Li, F. Y. Cheng, B. Guo and J. Chen, *J. Phys. Chem. B.*, 2005, **109**, 14017-14024.
41. D. Y. Wang, Z. X. Wang, X. J. Huang and L. Q. Chen, *J. Power Sources.*, 2005, **146**, 580-583.
42. Z. Wang, Z. Wang, H. Guo, W. Peng, X. Li, G. Yan and J. Wang, *J. Alloys Compd.*, 2015, **621**, 212-219.
43. M. Xu, L. Kong, W. Zhou and H. Li, *J. Phy. Chem. C.*, 2007, **111**, 19141-19147.
44. W. Wei, X. Cui, W. Chen and D. G. Ivey, *J. Phy. Chem. C.*, 2008, **112**, 15075-15083.

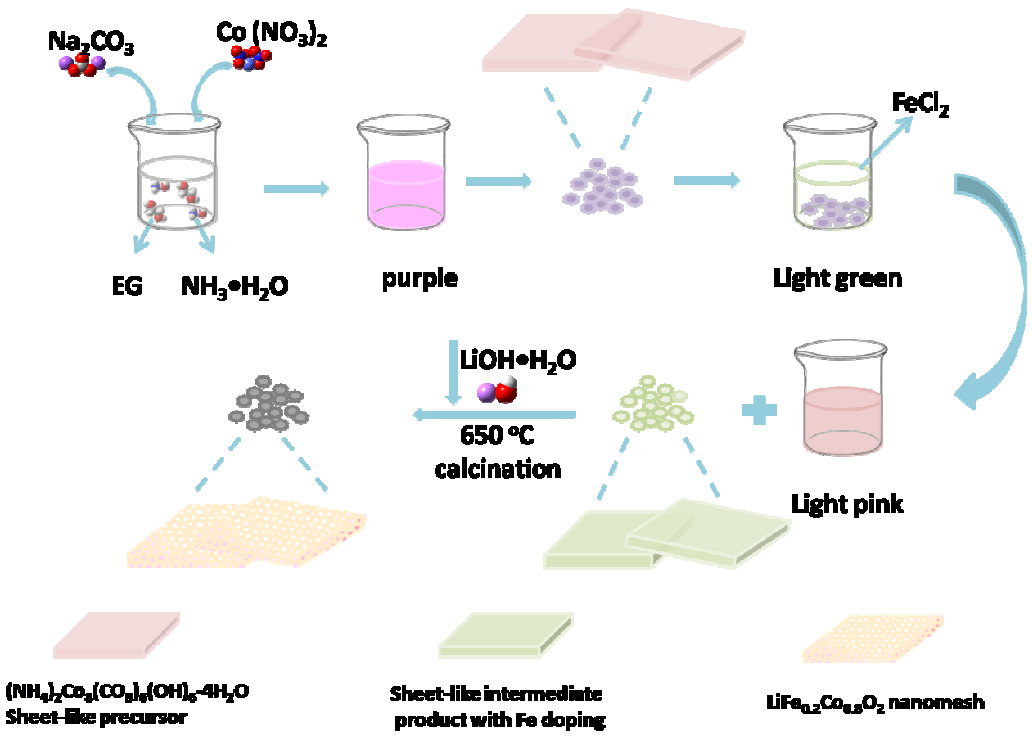

Scheme 1. illustration of the preparation process of 2 D LFCO nanomeshes.

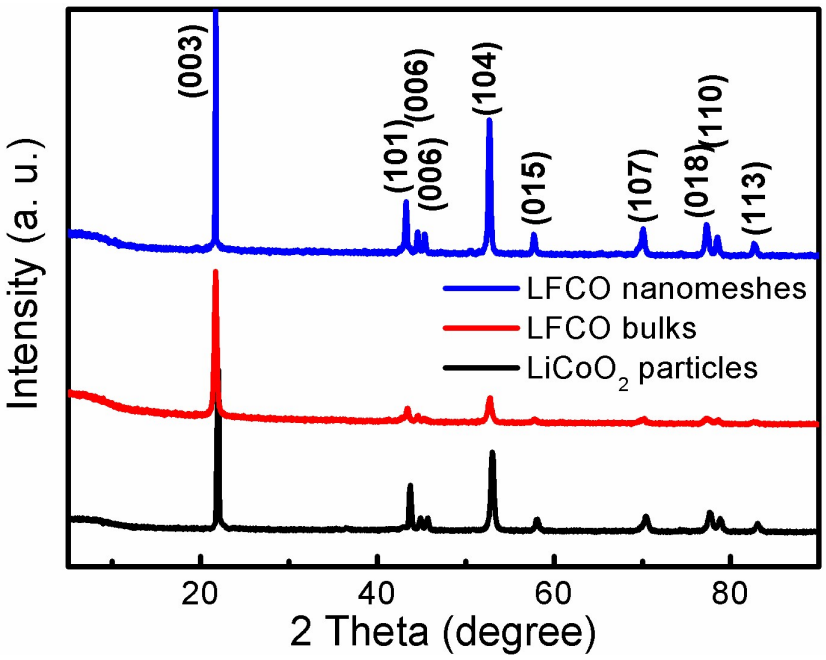

Fig 1. XRD patterns for $LiFe_{0.2}Co_{0.8}O_2$ nanomeshes, $LiFe_{0.2}Co_{0.8}O_2$ bulks and $LiCoO_2$ particles.

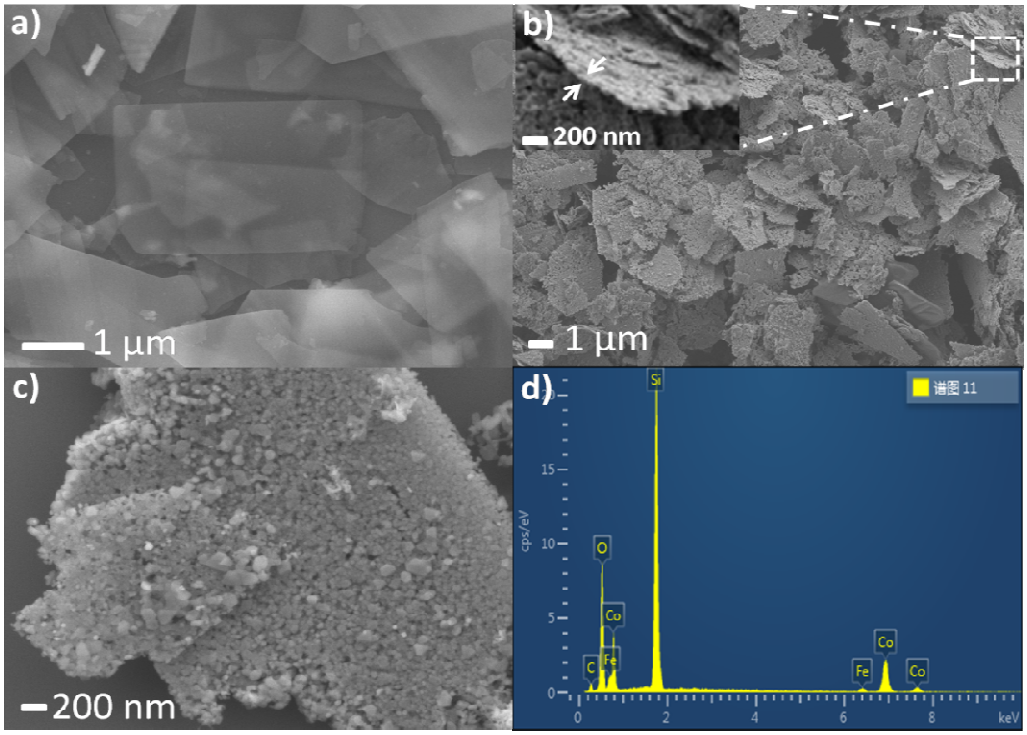

Fig 2. a) SEM image of the $(NH_4)_2Co_8(CO_3)_6(OH)_6{\cdot}4H_2O$ sheet-like precursors, b) SEM image of LFCO nanomeshes (the inset image is magnification SEM image of selected area), c) High-magnification SEM of individual LFCO nanomeshes, d) EDS image of LFCO nanomeshes.

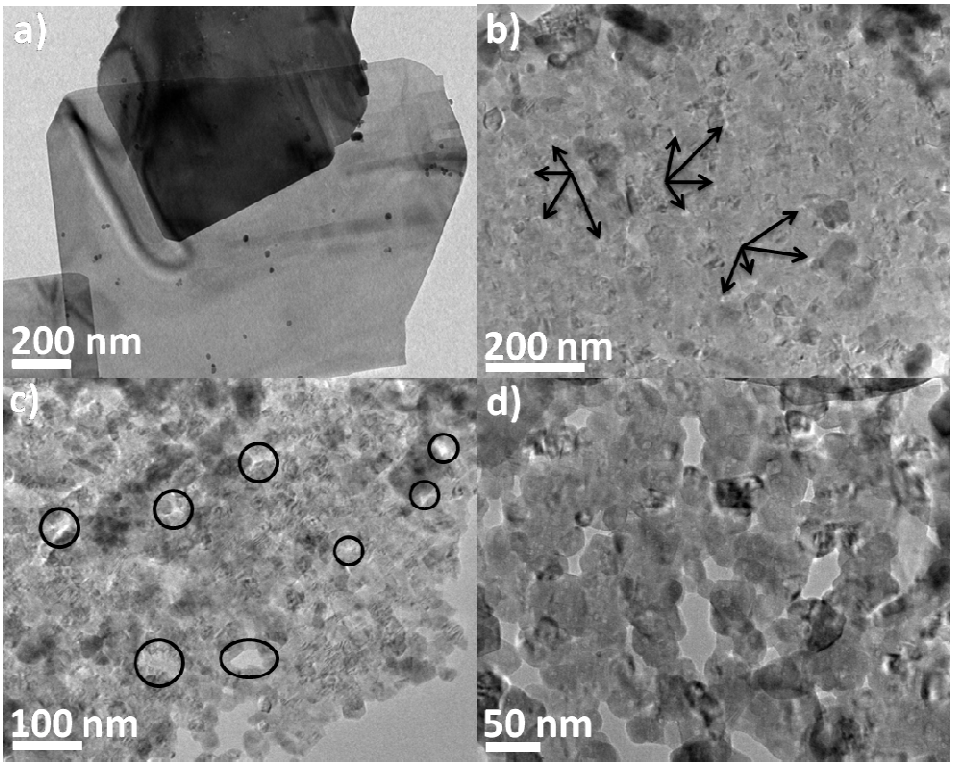

Fig 3. a) TEM image of sheet-like precursors, b-d) Stepwise magnified TEM images of LFCO nanomesh.

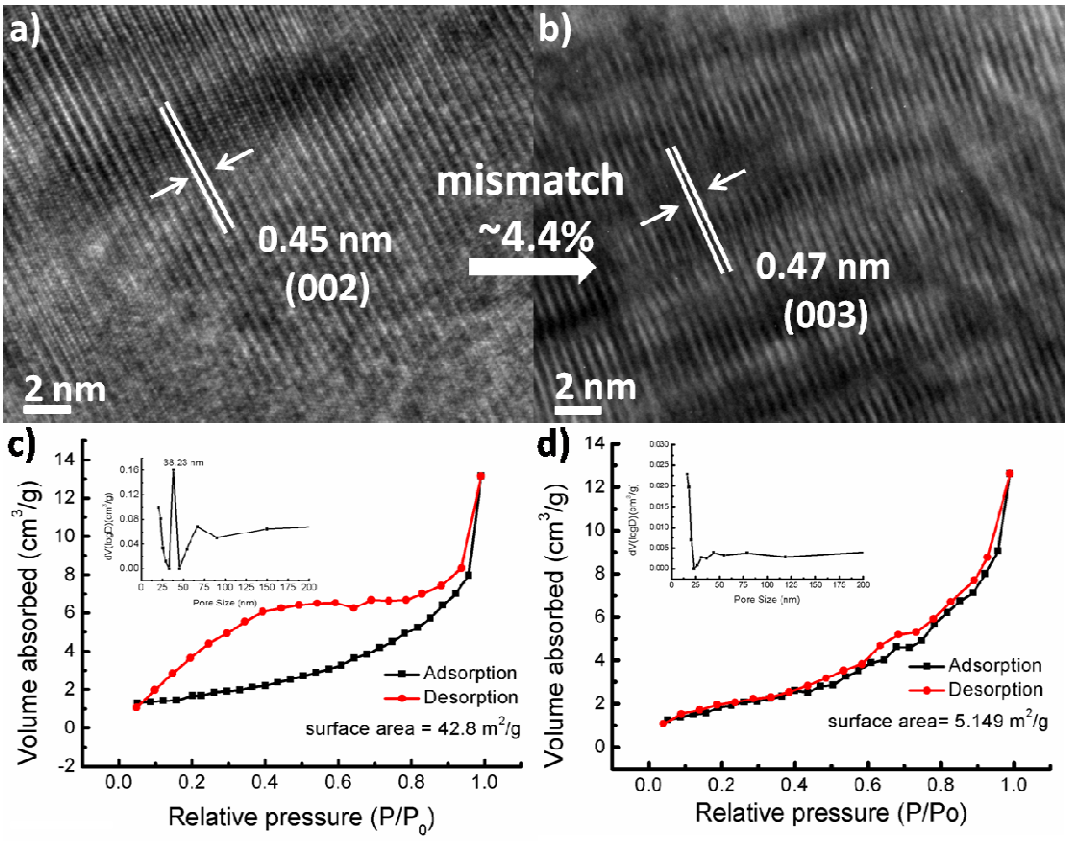

Fig 4. The locally magnified HRTEM image of a) sheet-like precursor and b) LFCO nanomesh, respectively. Nitrogen adsorption-desorption isotherm and the corresponding pore size distribution (inset) of c) LFCO nanomeshes and d) $LiCoO_2$ particles.

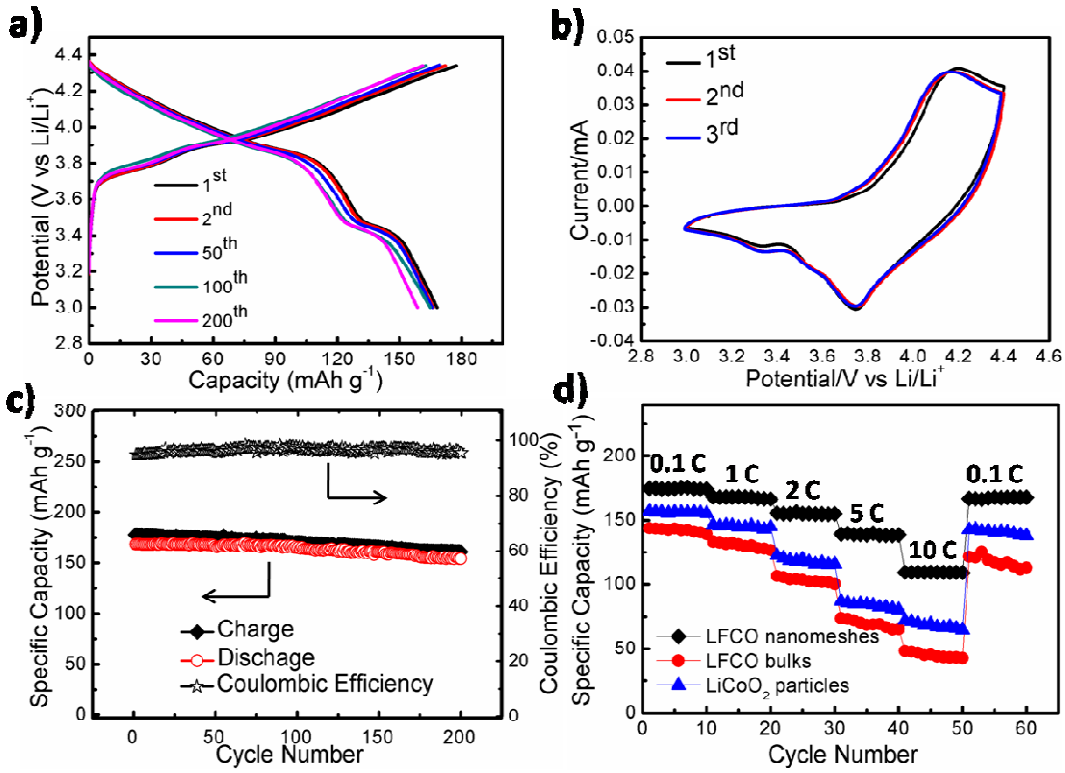

Fig 5. a) Galvanostatic discharge and charge curves in the voltage range of 3.0-4.4 V vs. Li at a charge current density of 0.1 C, b) Cyclic voltammetry (CV), c) The charge-discharge capacities and corresponding coulombic efficiency, d) Rate performance at different discharge rates, 0.1, 1, 2, 5 and 10 C, respectively, in the voltage range between 3.0 and 4.4 V of LFCO nanomeshes, LFCO bulks and $LiCoO_2$ particles.

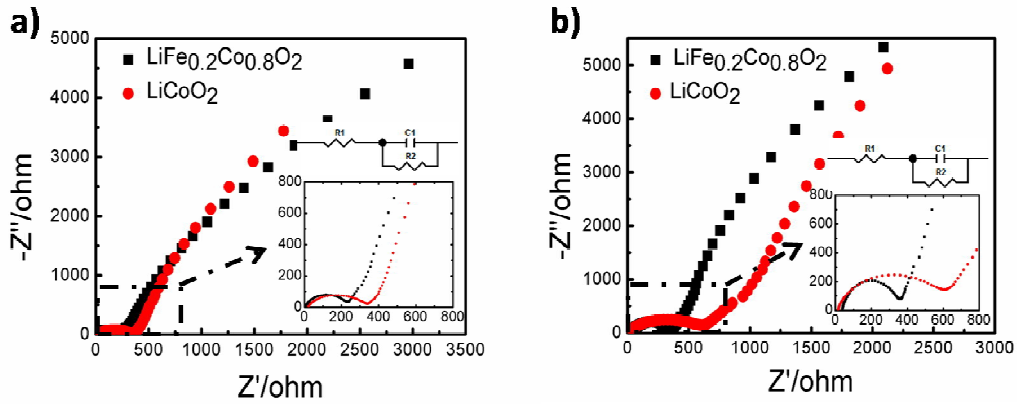

Fig 6. Niquist plots and the equivalent circuit images (inset illustration) of LFCO nanomeshes and $LiCoO_2$ particles for a) the first cycle and b) the 200th cycle.

Table 1. Resistance Values Obtained from Equivalent Circuit Fitting of Experimental Data for the LFCO nanomeshes and $LiCoO_2$ particles

Samlpe (Ω)	LFCO nanomeshes	$LiCoO_2$ particles
10th Rct	126.5	178
200th Rct	181.5	314